Advanced Optimization based on Bayesian Learning to Design Nonlocal Metasurfaces Deflectors for Satellite Communication

Ayoub Bellouch, Mahmoud Elsawy, Stéphane Lanteri, Erika Vandelle, Thi Quynh Van Hoang

Advanced Optimization based on Bayesian Learning to Design Nonlocal Metasurfaces Deflectors for Satellite Communication

Ayoub Bellouch Mahmoud Elsawy* Stéphane Lanteri Erika Vandelle Thi Quynh Van Hoang*

A. BELLOUCH, M. Elsawy, S. Lanteri
Université Côte d'Azur, Inria, CNRS, LJAD, 06902 Sophia Antipolis, France
Email Address: Ayoub.bellouch@inria.fr; mahmoud.elsawy@inria.fr
E. Vandelle, T. Q. V. Hoang
Thales Research & Technology, 1 avenue Augustin Fresnel, 91120 Palaiseau, France

Keywords: *Bayesian optimization (BO), Beam-steering Antenna, Efficient global optimization (EGO), Floquet Modes, Gaussian Process (GP), Ka-band, nonlocal Metasurfaces (NLMs), Phase Gradient Metasurface (PGMs), Satellite Communication (SatCom)*

An advanced optimization strategy is deployed to design high performance nonlocal metasurface deflectors, which are used as building blocks of a low-profile 2D-beam-steering-antenna in the Ka-band for SatCom. This new methodology combines two important ingredients. The first one is the nonlocal near-field effect generated by the interactions among adjacent sub-wavelength dielectric pillars. In this paper, we exploit this phenomenon, which was first investigated in the field of photonics, in the microwave domain. Moreover, we have advanced our approach by introducing non-uniformity in the lengths of the all-dielectric pillars. This enhancement has increased the degrees of freedom, offering a broader spectrum of design choices. These expanded choices lay the groundwork for the second ingredient: global optimization algorithm based on statistical learning to derive the geometrical characteristics of the constituting dielectric pillars, driven by a design objective. This optimization strategy delivers superior performance compared to the traditional global optimization algorithms and requires fewer solver calls. In this scenario, the deflector is specifically designed for Ka-band operation, achieving a 30° deflection angle at 30 GHz. The proposed solution demonstrates exceptionally high performance across the entire band of interest. The comparison between the optimized nonlocal metasurface deflector and its conventional counterpart, i.e. a phase gradient metasurface, shows numerous advantages, mainly in enhancing the diffraction efficiency, reducing the side lobes levels (SLL) and decriminalize the unwanted polarization. The experimental prototype confirms the results predicted by the simulation, highlighting the potential of this advanced optimization strategy for the design of high-performance beam-deflection systems.

1 Introduction

Beam-steering antennas embedded in Satellite-based communication systems (SatCom) on-the-move [1–3] aim to offer internet connectivity, facilitating information exchange with satellites, and ensuring secure communication for civil and military aircraft and vehicles on the move. These advancements are critical in the context of the rapidly growing demand for advanced connectivity and secure communication systems, driving progress in civil aviation, defense, and space exploration technologies [4]. These antenna systems are characterized by their ability to adjust their pointing direction, enabling coverage and scanning of a vast area from different angles in space. Conventional solutions of mechanical beam-steering, such as parabolic reflectors [5], are capable of delivering high performance, as evidenced by their widespread use in various applications, particularly in satellite TV reception. However, their cumbersome 3D architecture creates challenges regarding space constraints and aerodynamic issues [4, 6]. To circumvent these constraints, the objective is to innovate and develop alternative low profile beam-steering antennas that are cost-effective, low energy consumption and easy to manufacture, while ensuring robust performance standards. To this aim, a recent antenna architecture has been proposed, inspired by optical approaches based on Risley prism concept [7–10]. It consists of a planar radiating panel associated with two flat deflectors, whose rotations ensure the 2D-beam-steering capacity in elevation and azimuth planes.

To design beam-steering antenna systems with high-performance flat deflectors, recent approaches have increasingly turned to technologies based on metamaterials and metasurfaces due to their attractive features. Regarded as inhomogeneous sub-wavelength elements and arranged in repeating patterns, these materials can produce artificial electromagnetic (EM) properties [11–14], allowing control of phase, amplitude, and polarization [15–18]. In this regard, all-dielectric metasurfaces (ADMs) made from high-refractive-index materials have been suggested to design optical and millimeter-wave beam-steering systems with high performance [19–23]. Their all-dielectric nature ensures achieving high transmission efficiency responses over wider frequency bandwidth compared to other concepts such as impedance-sheet metasurfaces [24].

Hence, the fabrication of ADMs is facilitated by additive manufacturing [25], which offers many degrees of freedom for the design and moderate cost.

Recent metasurface beam-deflection solutions are often based on phase gradient metasurfaces (PGMs) concept. The conventional PGMs are constructed by arranging a linear array of subwavelength elements with a spatially-varying phase. This arrangement aims at creating a phase gradient in the transmitted far-field, enabling deflection control of the EM wave [26, 27]. In this configuration, the phase transformation is locally controlled by varying the dimensions of the motif through each unit-cell. This type of design is known as local metasurfaces, incorporates quasi-periodic sub-wavelength pillars, where each element generate independently its own scatterer response, considering the effects of adjacent cells as weak. Indeed, the overall structure performance is determined using a lookup table that dictates the properties of each element to align with the desired wavefront. On the other side, the nonlocal approach has newly emerged in the field of photonics [28–30]. It extends beyond the individual effects generated by each unit-cell, considering the interactions among adjacent sub-wavelength elements to shape the overall effective far-field response at the output of the structure. This nonlocal configuration provides a significant advantage by offering more degrees of freedom in the metasurfaces design, enabling new functionalities and extreme wave manipulation to optimize performance. Furthermore, this scenario enables reducing the complexity of the architecture, since specific requirements are not enforced on each sub-wavelength element, which potentially lead to design more efficient beam-deflection systems that are easier to manufacture.

In this paper, we leverage the recent progress in nonlocal metasurfaces (NLMs) concept in the optic and photonic fields to innovate efficient beam-deflection systems in microwave regime. In this sense, we exploit the significant artificial nonlocal interactions to attain superior functionalities, surpassing conventional designs. Moreover, we have overcome the bandwidth limitations encountered in studies on both local and nonlocal metasurfaces, achieving high transmission efficiency of the desired mode across the entire the Ka-Tx band for SatCom. To achieve this, we relied on recent progress in statistical learning-based optimization techniques to develop a methodology for optimizing the beam-deflection design. This type of method, called Bayesian optimization (BO) [31–33], employs cheaper surrogate model to replace the actual objective function, providing significant benefits for managing expensive and black-box functions, which is crucial due to the numerical complexity involved in accurately modeling nonlocal metasurface. To take advantage of this statistical approach, we have opted for one of the most advanced techniques belonging to the class of BO methods, known as Efficient Global Optimization (EGO) [32–38]. The EGO method is a global optimization algorithm that substitutes the complex and costly iterative electromagnetic evaluation process with a simpler and cheaper model. Contrary to the traditional global optimization strategies like Genetic Algorithms [38–40], the EGO method is not based on adaptive sampling, but on a surrogate model to build on a set of available fitness observations. This surrogate model utilizes a statistical learning criterion [41] related to the optimization target in order to identify which design should be tested in the next iteration that would provide better results close to the predefined goal.

As a result, we demonstrate here that our new approach optimizing the nonlocal effects of dielectric metasurfaces using the EGO method, can achieve superior deflector performance compared to conventional PGMs ones. Moreover, this adopted optimization methodology based on statistical learning ensures a significant reduction in the number of evaluations compared to traditional global optimization methods, thereby enhancing the potential to find promising solutions more rapidly, as illustrated by the deflector design proposed in this work. The rest of this article is organized as follows. The section II describes the design methodology for both the conventional PGMs and nonlocal metasurface deflectors, along with the optimization strategy adopted in this study. Section III presents the numerical results for the periodic cell and the finite deflector structure of the best design, with a comparison to the conventional one. In section IV, prototype measurements are carried out to validate the proposed design. The section V outlines the key conclusions.

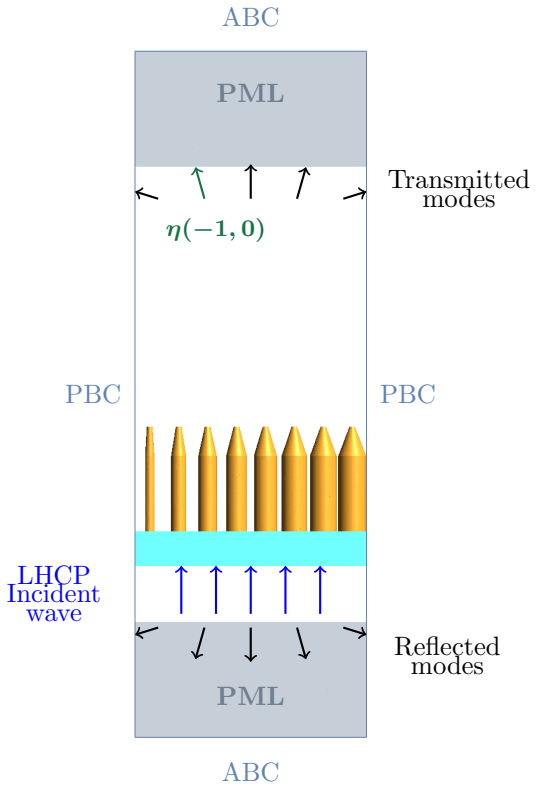

Figure 1: The periodic macro-cell of the deflector.

2 Design methodology

2.1 Macrocell configuration

In this work, our focus lies on periodic sub-wavelength deflectors composed of macrocells repeated in two dimensions, along the x- and y-axes. Applying the grating law for a normal incident wave, the period Λ of the sub-wavelength deflector can be calculated for the mth diffraction order and the desired angle α at the design wavelength λ_0, as follows:

$$\Lambda = \frac{m\lambda_0}{\sin(\alpha)}. \tag{1}$$

Our target deflector is designed to generate the first-order mode at a desired deflection angle around $\alpha = 30^\circ$ at the ka-Tx band for SatCom. By applying equation (1) for the frequency $f_0 = 30\,\text{GHz}$, the period along x-axis P_x is equal to $\Lambda = 20\,\text{mm}$. The period along y-axis is chosen $P_y = 2.6\,\text{mm}$, sufficiently small compared to the operating wavelength. A composite material with high permittivity ($\epsilon_r = 8.5$) is used for the cylindrical all-dielectric pillars. A matching layer with pyramidal shape is added above the pillars to improve the transmission efficiency. Additionally, a substrate support base is used to ensure the mechanical rigidity of the deflector, with a low permittivity material ($\epsilon_r = 2.3$) in order to minimize the reflection.

On the other hand, given that the deflector is composed of repeated macro-cell in two dimension, it will be modeled as an infinite periodic structure with periodic boundary conditions (PBCs). Moreover, a perfectly matched layers (PMLs), along with absorbing boundary conditions (ABCs), are applied to the top and bottom of the structure to prevent parasitic reflections and accurately model the far-field behavior away from the structure. Therefore, we can describe how the transmitted far-field is split into diffraction orders by using Floquet modal decomposition theory, which in the present case amounts to define and compute the mode diffraction efficiencies $\eta(m, n)$ in Ka-Tx band frequency range. An illustration of the periodic macro-cell of the deflector in its simulation configuration is shown in Fig 1. A left-handed circularly polarized (LHCP) plane wave is used as incident wave, excited at the lower Floquet port. Hence,

the diffraction efficiencies of the modes are computed at the upper Floquet port. This macrocell full-wave configuration is commonly employed in simulating both conventional and nonlocal deflectors.

2.2 Conventional sub-wavelength deflector

To generate the beam deflection, in conventional sub-wavelength deflectors, the required phase profile along the deflection plane (along the x-axis, for example) is calculated inside each macrocell for the desired deflection angle at the design wavelength using:

$$\varphi(x) = \frac{2\pi}{\Lambda}x \tag{2}$$

Sub-wavelength pillars with varying diameters are used to generate the desired phase profile. Indeed, by changing the pillar diameter, we can locally control the effective refractive index, thus the phase shift. A numerical analysis was done to calculate the phase shift based on the variation of the pillar's diameter within the pillar's unit cell, using periodic boundary conditions. Hence, a complete 360° cycle can be obtained by varying diameters of the pillars. In our study, we constructed a classical PGM deflector with a fixed pillar total heights of 9mm, including cone heights of 2.5mm, and varying diameters ranging from 0 to 2.6 mm to cover all the phase distribution in the Ka-Band. This conventional sub-wavelength deflector, used as a design example in the macrocell of Fig 1, will be compared with the optimal design of the NLM configuration, which will be obtained using our optimization strategy.

2.3 Nonlocal metasurfaces design

The nonlocal effect occurs when the sub-wavelength pillars are coupled. The behavior of each element is influenced by the state of its neighboring ones. In this scenario, components not only interact with the external waves directly incident upon them but also with the waves coming from adjacent metasurfaces, resulting in a complex near field coupling effect. This inter-element interaction significantly impacts the overall behavior of the macro-cell, referred to as the effective response. In order to introduce this phenomenon, we will deviate from classical phase-gradient approaches based on generating field distribution element by element. This entails first granting the pillars the freedom to move within the grid to create the desired couplings effects and also breaking the uniformity of element heights imposed before by the permittivity of the dielectric pillars. This novel non-uniform configuration, to the best of our knowledge, has not been previously introduced in the literature.

On the other hand, to model the nonlocal metasurface deflectors and, more importantly, to effectively capture the strong near-field coupling generated by the elements, a full-wave approach was utilized to simulate the deflector by solving the complete system of Time-domain Maxwell equations. For this purpose, we exploit a Discontinuous Galerkin Time-Domain (DGTD) solver that we have recently developed [42,43] and which is implemented in our in-house simulation software called the DIOGENeS [44]. In this simulation configuration, cylindrical sub-wavelength pillars are employed, with only 5 pillars per period, compared to the 7 or 8 typically employed in conventional approaches to cover the total phase-shift range and to reduce the phase quantization error. Since the focus is not on the phase-gradient distribution, we can take advantage of this to create a lightweight structure and enhance the freedom of position within the macrocell for the dielectric pillars. Details about the choice of those parameters will be discussed in Section III-A.

2.4 Optimization strategy

An inverse design problem is formulated to optimize the deflector's macro-cell structure. In the present case, the objective is to enhance the diffraction efficiency $\eta(-1,0)$ in the desired diffraction mode order $(-1,0)$, which corresponds to the desired angle of the beam steering, while concurrently minimizing the efficiency level for other diffraction modes. An additional aim is to minimize the ratio between the co- and cross- polarizations. Hence, this optimization problem seeks to determine the positions and dimensions

of cylindrical pillars that achieve the best performance by minimizing a cost function. Here, we taked advantage from the nonlocal effect to offer the optimization process more degrees of freedom in the choice of the design dimensions. The parameters $\mathbf{X}$ to be optimized include the radius $r_{i\in[\![1,n_p]\!]}$, total height of pillars $h_{i\in[\![1,n_p]\!]}$, height of cones h_c and distance between consecutive pillars $d_{i\in[\![1,n_p-1]\!]}$, leading to $3n_p$ optimized parameters, with n_p is the number of pillars. To construct the objective function, it is necessary to incorporate the two key performance elements mentioned previously. The principal objective is to increase deflection efficiency of the mode $(0,-1)$, but more importantly to maximize the efficiency $\eta_{LHCP}(0,-1)$ of the LHCP polarization to maintain the same polarization as the incident wave. The second related objective is to minimize the Axial Ratio (AR), i.e. the ratio between the major and minor axes of an elliptical polarization (EP). The idea is to ensure a CP nature of the transmitted wave, because the configuration of the pillars does not necessary preserve the nature of the incident wave polarization. By minimizing the AR factor, we will simultaneously raise the cross-polarization discrimination (XPD), which is the ratio between the co- and cross-polarizations, which allows to decriminalize the unwanted polarization RHCP. The relation between the AR and XDP ratios is given by the following formula :

$$AR = \frac{\text{Major axis}}{\text{Minor axis}} = \frac{XPD+1}{XPD-1} \in [1,+\infty[\,, \tag{3}$$

with $XPD = \sqrt{\dfrac{\bar{\eta}_{LHCP}(-1,0)}{\bar{\eta}_{RHCP}(-1,0)}}$

In order to achieve the desired performance, the two related objectives, i.e. the $\eta_{LHCP}(-1,0)$ diffraction efficiency and the AR factor, can be combined into the same cost function to be minimized. Thus, the optimization problem to solve can be written as:

$$\text{Minimize} \quad f_n(\mathbf{X}) = \frac{1}{2}\left(2 - \bar{\eta}_{LHCP}\,(-1,0) - \frac{1}{AR^n}\right) \in [0,1] \tag{4}$$

where n is the exponent order, adjusting the weighting of the AR in the objective function. Solving this inverse design requires a rigorous and computationally efficient optimization strategy, which is capable of treating several design parameters while minimizing solver calls. For this purpose, we consider here the EGO method, introduced in section I, which belongs to the class of BO statistical learning approach. This choice is made to significantly reduce the number of function evaluations needed compared to conventional optimization techniques, which is crucial to handle with our sophisticated 3D structure. In practice, the EGO is based on two phases. The first one is the design of experiment (DOE), in which an initial database is generated. In essence, a uniform sampling strategy is deployed in order to generate different designs in which the cost function is evaluated using our electromagnetic DGTD solver. In the second phase, a Gaussian process (GP) model is constructed to fit the data obtained from DOE. This GP model allows us to predict the values of the cost function in the parameter space without the need to perform additional simulations. Therefore, one can estimate at any point of the design space, the objective function (mean of the GP model) and an uncertainty value (variance of the GP model). The mean and the variance are used together to determine a statistical merit function. In our case, we rely on the expected improvement, which is a function whose maximum defines the next design parameters set to be evaluated. That is to say, in the search parameter space where this function is maximized, we extract the corresponding parameter values, and the corresponding design will be simulated using the DGTD solver. Then the database is updated accounting for this new observation (construction of a new GP model based on the updated database). We repeat this process until a predefined convergence criterion is reached, or when the expected improvement is sufficiently small.

3 Numerical results

3.1 Macro-cell optimization results

The aim of optimization is to find the most efficient arrangement of the metasurface pillars to enhance the performance of the deflector within the whole SatCom Ka-Tx band, covering the frequency band from 27.5 to 31 GHz. The desired deflection will be provided by the effective behavior of the entire macro-cell due to the near-field coupling between pillars, and not by the local effect generated by a distinctive pillar with specific dimensions as in the conventional case. In this configuration, the objective function $f_n(\mathbf{X})$, described in (4), is optimized with a value $n = 2$ to provide an adequate weighting between the two related objectives. The number of pillars used here is $n_p = 5$ per period, leading to 15 parameters of optimization.

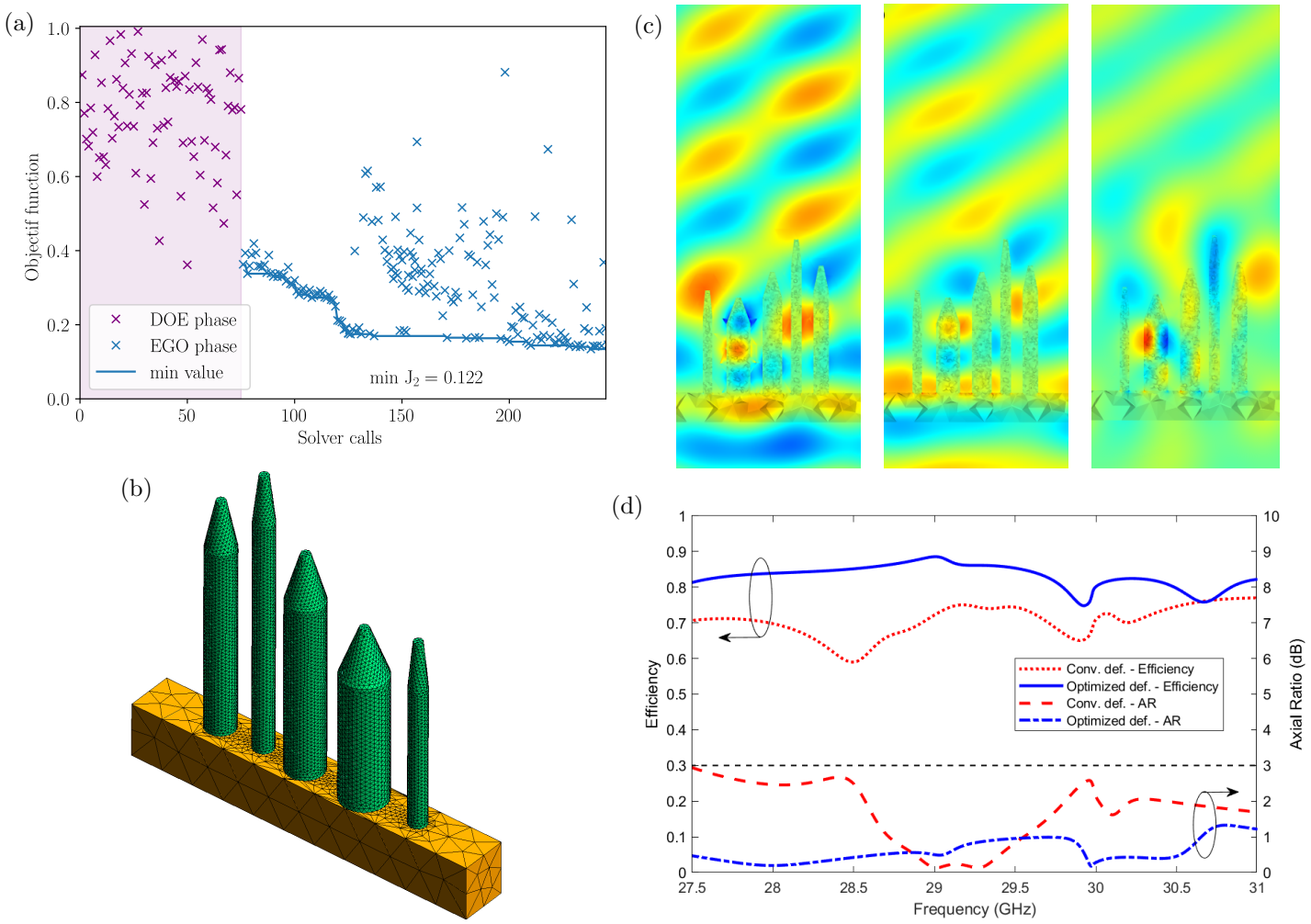

Figure 2: Optimization using the EGO method (a) Evolution of the objective function with the number of full-wave solver calls, (b) The best design, (c) Field maps of $Re(E_x)$, $Re(E_y)$ and $Re(E_z)$ obtained for the optimized design at $f_0 = 29GHz$, (d) Comparison between a conventional design (red curves) and an optimized design (blue curves): performance of the macrocell in efficiency and Axial Ratio versus frequency.

As explained previously, the optimization has been realized using the EGO method. During the first phase, we build a DOE database with 75 points. It represents five times the number of parameters, which is sufficient to construct an initial GP surrogate model. In the second phase, i.e., the EGO phase, this surrogate model is refined during the optimization process to find a global minimum. Figure 2.a summarizes the optimization process, in which the objective function evaluations of the DOE are displayed with purple points and the evaluations obtained during the EGO phase are displayed with green points. The deflector designs have been evaluated using the a DGTD-$\mathbb{P}_2$ method where $\mathbb{P}_2$ refers to the second-order polynomial interpolation used for the DG discretization. The optimal design found by optimization is shown in Fig 2.b.

It was reached after only 240 iterations, despite the high number of parameters. The optimization results confirm that the EGO algorithm facilitates achieving convergence with much fewer iterations compared with traditional optimization algorithms. Furthermore, it is clear that the configuration of the obtained design, as shown in Fig 2.b, differs from those produced by traditional PGMs methods. First, the periodicity between the pillars is no longer maintained, and the diameters of the pillars do not adhere to the phase gradient. Additionally, the heights of the pillars are not uniform, which introduces a novel aspect that, to the best of our knowledge, has not been previously explored in the literature on beam-deflection systems. Furthermore, the near-field coupling between pillars enhances the overall effective deflection in the far-field. This nonlocal phenomenon is illustrated in the field maps presented in Fig 2.c. These outcomes offer a comprehensive view of the non-intuitive interactions among pillars, revealing how the collective behavior shapes the overall characteristics observed in the far-field pattern.

The results, depicted in Fig. 2.d, represent the performance of the macro-cell configuration across all frequencies of the Ka-Tx band. A comparison was made between the optimal design from the EGO algorithm shown in Fig. 2.b and represented by the blue curve in Fig. **??** and the conventional design based on phase-gradient shown in the Fig. 1 and represented by the dashed red curve in Fig. **??**. In terms of co-polarization efficiency, the optimal design achieved notably high values, reaching approximately 80% with a stable level across the entire band, compared to around 65% for the conventional design with fluctuations in some areas. On the other hand, the optimal design achieved very low levels of AR, falling below the imposed threshold of 1.5 dB, whereas the gradient-phase design only adhered to this threshold within a limited frequency range around 29GHz. Hence, this nonlocal approach offers a more efficient solution than the conventional phase-gradient strategy.

3.2 Finite structure performance

The current step involves validating the results for the finite structure without periodic boundary conditions to carefully consider the influence of edge effects. We constructed finite structures with a 260 mm diameter, corresponding to 13 macrocell periods, a dimension deemed sufficiently large to approximate the behavior of an infinite deflector in a periodic environment. The total diameter of the deflectors is 280 mm, consisting of a 260 mm effective surface and a 20 mm fixation section.

The designs for both conventional and optimized deflectors are illustrated in Fig. 3(a) and (b). Deflector functionality was evaluated by illuminating each one with a left-handed circularly polarized (LHCP) Gaussian source at normal incidence. The LHCP co-polarization efficiency and Axial Ratio (AR) of both designs were evaluated using the Transient solver of the CST microwave suite. The efficiency calculation involved three parameters: the directivity of the standalone LHCP Gaussian source, the directivity of the system comprising the LHCP Gaussian source and a deflector, and the cosine of the deflection angle (which is 30° at 30 GHz). Fig. 3(c), (d) and (e) present a comparative analysis of the far-field radiation patterns for the two deflectors at 28 GHz, 29 GHz and 30 GHz, respectively. The results indicate that the optimal design given by the EGO achieves enhanced directivity of approximately 1 dB in the desired direction. The optimized design also exhibits a notable reduction in side lobes levels (SLL) and a significant minimization of the RHCP cross-polarization when compared to the phase-gradient conventional deflector.

Fig. 3(f) and (g) depict the performance of the finite structures in terms of LHCP co-polarization transmission efficiency and AR across the frequency range of interest from 27.5 to 31 GHz. The optimized deflector demonstrates a notably high efficiency, exceeding 80%, while maintaining a robust circular polarization with an AR less than 1 dB throughout the entire Ka-Tx band (27.5 GHz to 31 GHz). Overall, the optimized deflector features superior performance relatively to its conventional counterpart. The results obtained with the macrocell configuration are also diplayed on the graphs, showing that the finite structure achieves similar results, thereby validating the adopted modeling approach.

The AR results confirm that the finite structure's performance aligns closely with the macrocell's, even though AR levels are highly sensitive to various factors such as the strong near-field coupling between pillars and edge effects. Despite these sensitivities, the optimized deflector maintains values below the 1.5 dB-threshold across the entire frequency range of interest, outperforming the conventional design in circular polarization quality.

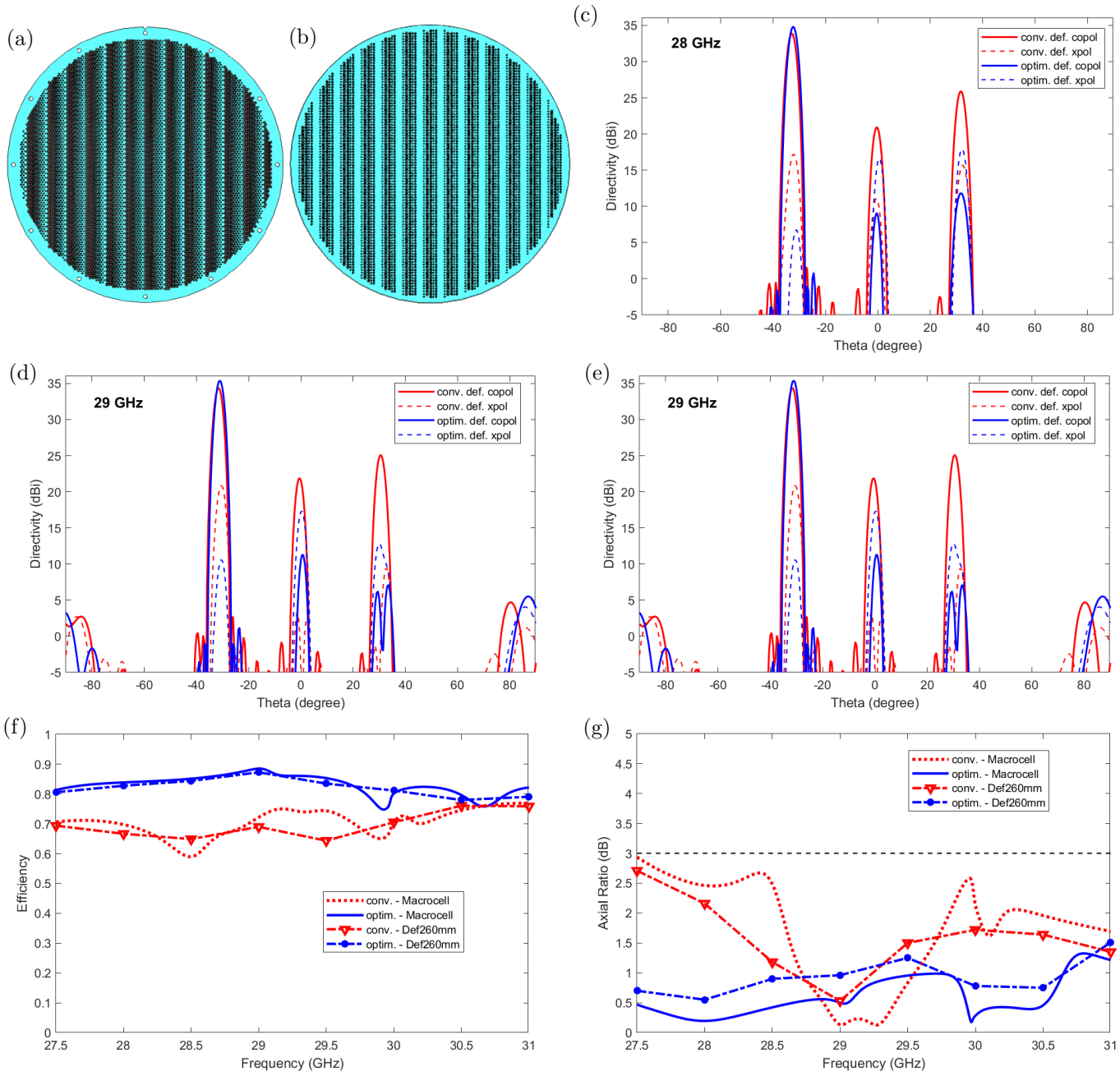

Figure 3: Finite structures of 260 mm diameter: (a) Conventional deflector, (b) Optimized deflector; Comparison of radiation patterns of the conventional deflector (red curves) and the optimized deflector (blue curves) illuminated by an LHCP Gaussian source: (c) at 28 GHz, (d) at 29 GHz, (e) at 30 GHz. Performance of the macrocell and the finite 260mm-diammeter structure : conventional deflector (red curves) and optimized deflector (blue curves) (f) Efficiency of the LHCP co-polarization component, (g) Axial Ratio versus frequency.

These findings highlight the advantages of the nonlocal design in achieving enhanced and reliable radiation performance. They also validate the modeling approach, demonstrating that macrocell simulations can reliably predict the performance of sufficiently large finite structures (from approximately ten periods). This insight is crucial, as it enables efficient macrocell optimization with high confidence in the expected performance of the corresponding finite structure, significantly saving time and computational resources during design and optimization stage.

4 Prototyping and measurement

For experimental validation, only the optimized deflector was manufactured. This component was fabricated using Zetamix Epsilon filament [45] and an advanced FDM-based 3D printing technique tailored for metasurfaces based on subwavelength cylindrical pillars [46]. A photograph of the fabricated deflector appears in Fig. 4(a).

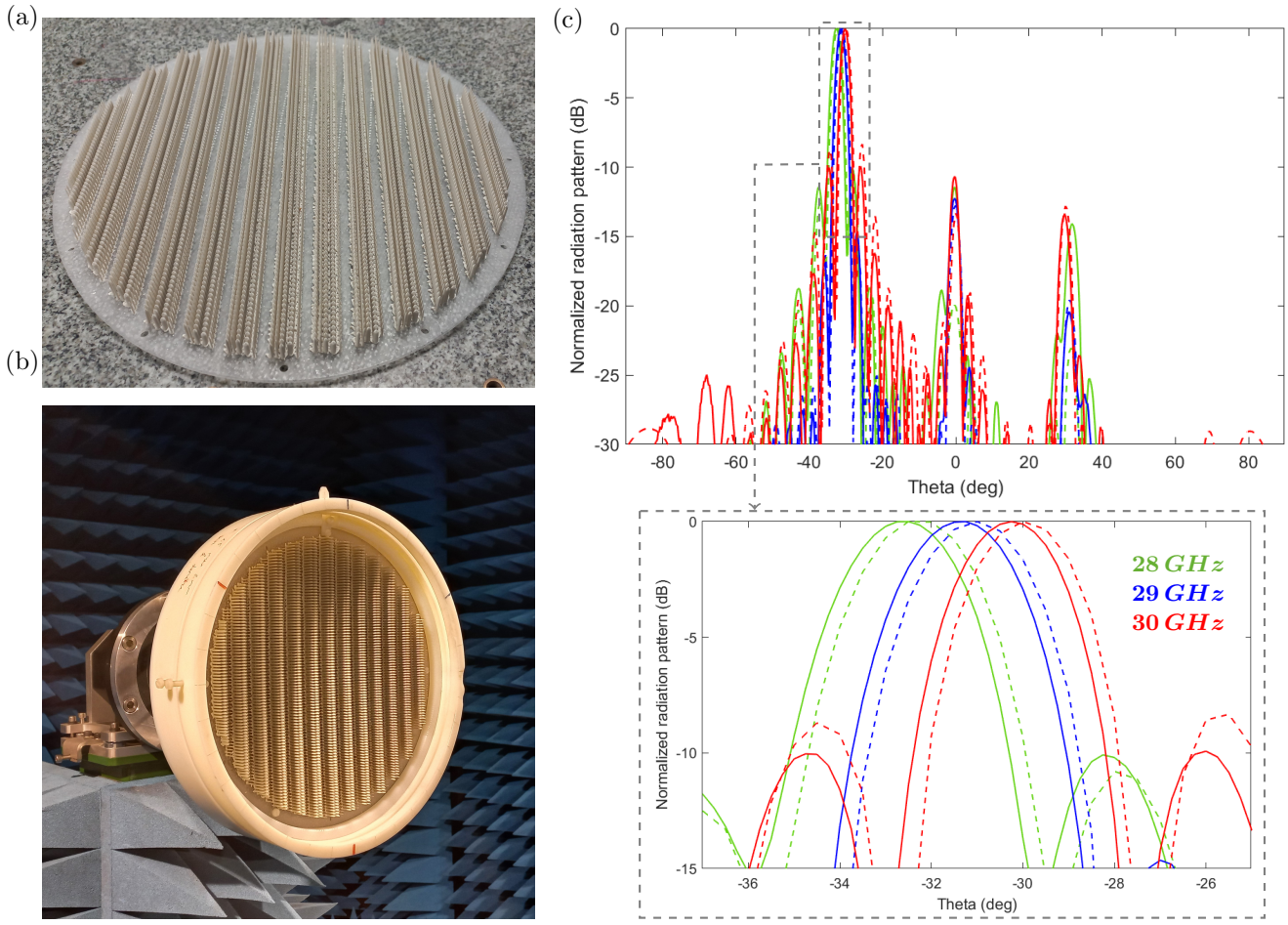

Figure 4: (a) Manufactured 260mm-diameter deflector, (b) RLSA combined with the optimized deflector in an anechoic chamber, (c) Radiation pattern of CRLSA combined with the optimized deflector: (a) Simulation (dashed lines) and measurement (solid lines) results of cut planes at 28, 29, 30 GHz.

In the previous section, the optimized deflector was evaluated by using an ideal Gaussian source as illuminator. However, in practice, the optimized deflector was illuminated by a circularly polarized RLSA [47]. The gap between the RLSA and the deflector was set to 5 mm, corresponding to half the wavelength at 30 GHz. It is important to note that the RLSA possesses a narrower bandwidth than the Gaussian source, which limits our ability to evaluate the wideband behavior of the optimized deflector. Additionally, the circular polarization of the RLSA is not as ideal as that of the Gaussian source, resulting in a slightly higher axial ratio when the optimized deflector is combined with this source compared to the performance

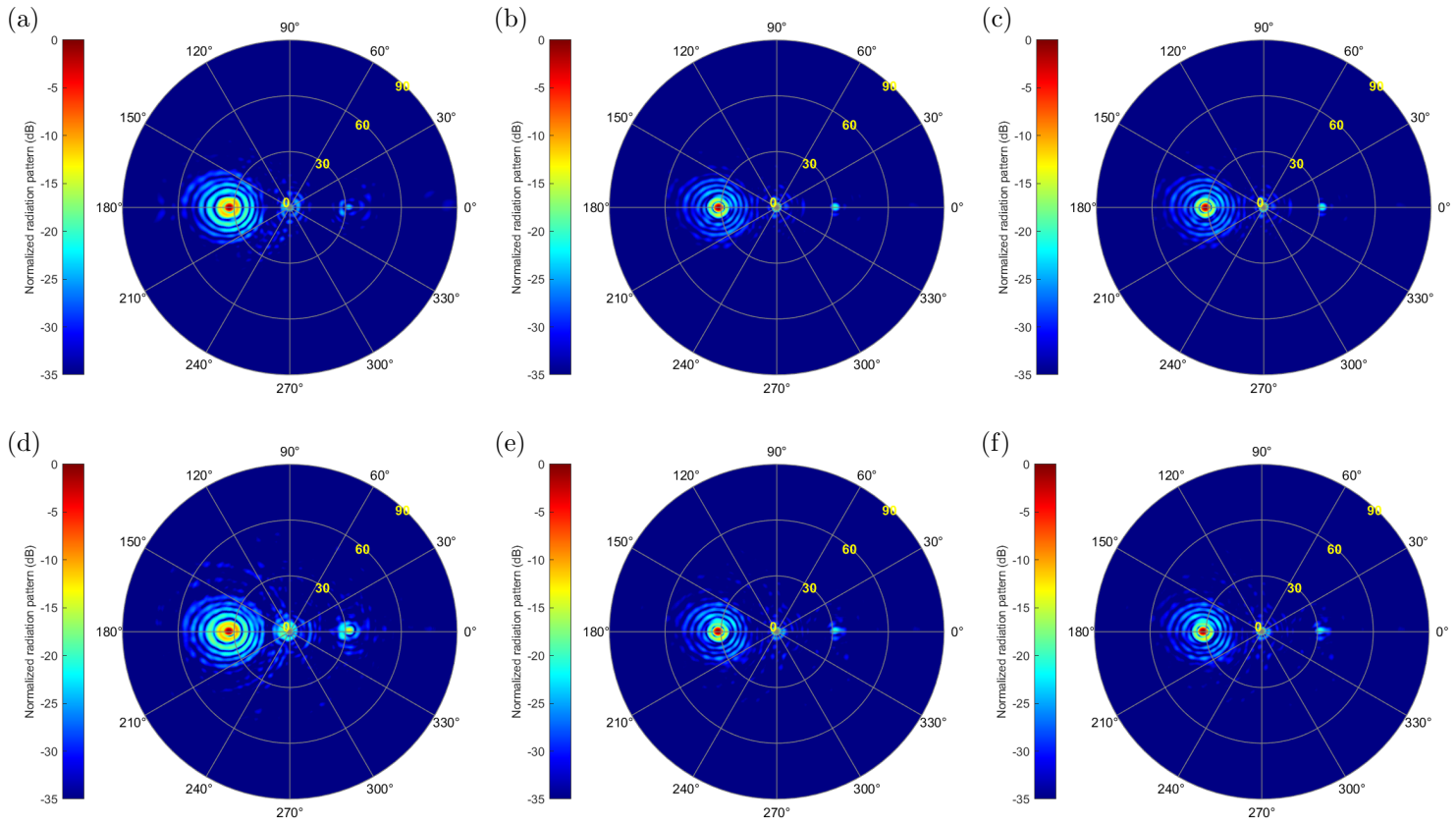

Figure 5: 3D radiation pattern : simulation result at (a) 28 GHz, (b) 29 GHz, (c) 30 GHz, and measurement result at (d) 28 GHz, (e) 29 GHz, (f) 30 GHz.

obtained with the Gaussian source. The performance of the complete antenna, consisting of the RLSA and the optimized deflector, was evaluated in CST Microwave Studio 2021 using the Finite Integration Technique (FIT) Transient Solver. The radiation pattern measurements were conducted by mounting the entire system on a multi-axis positioner in an anechoic chamber, as shown in Fig. 4(b). Measurements were conducted over the frequency range of 27 GHz to 31 GHz, using a dual-polarized circular waveguide as the probe and a SATIMO QR18000 as the gain reference antenna. Angular measurements were taken in steps of 0.25° for elevation and 0.5° for azimuth. The measurement was performed in the near-field region at a distance of 3.0 meters, and the collected data were subsequently transformed to the far-field to obtain the radiation patterns. Fig. 4(c) compares the simulated and measured radiation patterns in the deflection plane at 28, 29 and 30 GHz. The main beam direction and grating lobes positions show good agreement between simulation and measurement. These directions correspond to the diffraction orders angles of the periodic deflector and can be analytically calculated by equation (1). The angle dispersion in frequency is 1°/GHz, derived from the relationship between deflection angle and frequency for a given deflector period, as shown in equation (1).

Fig. 5(a) and (b) present the normalized 3D radiation patterns at 29 GHz, revealing a close alignment between simulation and measurement across the entire 3D pattern. The energy is concentrated in the main beam at a deflection angle of 31°, with a 3dB-beamwidth of approximately 2.75° in both simulation and measurement. While the measured diffused level is slightly higher than in the simulation, it remains below –10 dB relative to the main lobe.

Fig. 6 illustrates the measured realized gain of the LHCP co-polarization and the Axial Ratio across frequencies, alongside the standalone RLSA results. The 3dB frequency bandwidth is 6.4%, covering the range from 27.9 to 29.75 GHz. This bandwidth primarily depends on the radiating panel that illuminates the dielectric deflector. Recent advancements in corporate-feeding slot arrays and open stub arrays have shown great potential to widen the frequency bandwidth.

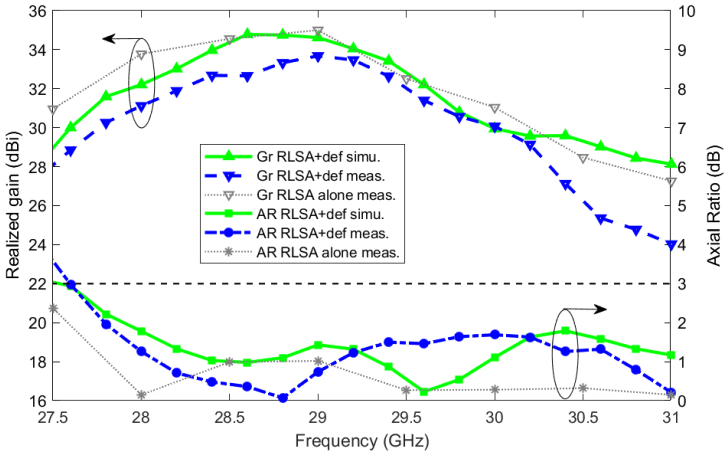

Figure 6: RLSA combined with the optimized deflector – Simulation (green curves) and measurement (blue curves) results: Realized gain and Axial Ration versus frequency. The measured results of the RLSA alone are shown in gray curves.

Realized gain measurements match the simulation well up to 30 GHz; beyond this frequency, the measured gain drops rapidly, diverging by 3dB from the simulated gain at 31 GHz. Ongoing investigations aim to identify the cause of this discrepancy. The Axial Ratio shows similar behavior in both simulation and measurement, with the lowest values at 29.6 GHz in the simulation and at 28.8 GHz in the measurement. This frequency shift may stem from differences between the simulated and actual permittivity of the fabricated component. Overall, the measurement results align well with the simulation.

5 Conclusion

In this paper, we introduced the nonlocal metasurface concept within beam-deflection systems operating in the microwave regime, paving the way for the development of high-performance deflector designs. As discussed in this study, employing the near-field interactions unlocks new systems functionalities and extreme wave manipulation. This advantage was combined with an advanced optimization strategy based on statistical learning to offer the potential to determine optimal solutions with a reasonable number of full-wave solver iterations. The EGO algorithm, based on Gaussian process learning, enables fast and robust predictions of the objective function, facilitating the determination of highly efficient designs within a reasonable computation time. As highlighted, this optimization strategy outperforms evolutionary algorithms and local gradient techniques by minimizing the number of iterations needed to reach convergence.

The optimized design proposed here with only 5 cylindrical pillar per macro-cell offers a significant efficiency increase of the $(-1, 0)$ transmitted mode of the circularly polarized incident wave, coupled with an important axial ratio reduction between co- and cross-polarizations across the Ka-Tx band compared to conventional designs. Furthermore, the radiation pattern results of the complete deflector demonstrate remarkable performance gain, reduced unwanted radiation, and overall improved efficiency. The measurement results confirm the simulated performance of the nonlocal metasurface deflector, demonstrating the advantages of this design approach in achieving lightweight, low-cost, low-profile beam-deflection systems. This facilitates the development of antenna systems equipped with efficient deflectors capable of 2D-beam-steering with wide field-of view. This makes these systems perfectly suited for SatCom on-the-move applications, as they guarantee reliable wave transmission and ensure strong connectivity.

6 Experimental Section

First part of experimental section:
Second part of experimental section:

Supporting Information
Supporting Information is available from the Wiley Online Library or from the author.

Acknowledgements
Please insert your acknowledgements here

References

References

[1] Y. Jiang, S. J. Foti, A. Sambell, and D. Smith, "A low profile radiating element with nearly hemispheric coverage for satellite communications on-the-move hybrid array antenna," in *Proc. CSNDSP, Newcastle upon Tyne, U.K.*, Jul. 2010, pp. 123–127.

[2] Z. Wu, M. Yao, H. Ma, W. Jia, and F. Tian, "Low-cost antenna attitude estimation by fusing inertial sensing and two-antenna GPS for vehicle-mounted satcom-on-the-move," *IEEE Trans. Veh. Technol.*, vol. 62, no. 3, pp. 1084–1096, Mar. 2013

[3] Satcom-on-the-move: A Terminal Engineered to Sing, *https://www.emsolutions.com.au/wp-content/uploads/Satcom-on-the-move-terminal-engineered-to-hum.pdf.*

[4] F. Ahmed, K. Singh, and K. P. Esselle, "State-of-the-art passive beam-steering antenna technologies: Challenges and capabilities," *IEEE Access.*, vol. 11, pp. 69101-69116, May. 2023.

[5] A. W. Rudge and M. J. Withers, "New technique for beam steering with fixed parabolic reflectors," *Proc. Inst. Electr. Eng.*, vol. 118, no. 7, pp. 857–863, Jul. 1971.

[6] P. J. B. Clarricoats and A. D. Olver, "Corrugated Horns for Microwave Antennas," no. 18. Edison, NJ, USA: IET, 1984.

[7] S. D. Risley, "A new rotary prism.," *Transactions of the American Ophthalmological Society.*, vol. 5, no. 3, p. 412, 1889.

[8] Y. Yang, "Analytic solution of free space optical beam steering using Risley prisms," *J. Lightw. Technol.*, vol. 26, no. 21, pp. 3576–3583, Nov. 2008.

[9] Y. Lu, Y. Zhou, M. Hei, and D. Fan, "Theoretical and experimental determination of steering mechanism for Risley prism systems.," *Appl. Opt.*, vol. 52, no. 7, pp. 1389–1398, 2013.

[10] J. Wang and Y. Ramhat-Samii, "Phase method: A more precise beam steering model for phase-delay metasurface based Risley antenna.," in *Proc. URSI Int. Symp. Electromagn. Theory.*, pp. 1–4, May. 2019.

[11] G. V. Viktor, "The electrodynamics of substances with simultaneously negative values of ϵ and μ," *Soviet Physics Uspekhi.*, vol. 10 no. 4, pp. 509-514, Apr 1968.

[12] D. R. Smith, W. J. Padilla, D. C. Vier, S. C. Nemat-Nasser, and S. Schultz, "Composite Medium with Simultaneously Negative Permeability and Permittivity," *Phys. Rev. Lett.*, vol. 84, no. 18, pp. 4184-4187, 2000.

[13] R. W. Ziolkowski, and E. Heyman, "Wave Propagation in Media Having Negative Permittivity and Permeability," *Phys. Rev. E, Stat. Phys. Plasmas Fluids Relat. Interdiscip. Top.*, vol. 64, no. 5, p. 056625, Dec 2001.

[14] A. Sihvola, "Metamaterials in electromagnetics," *Metamaterials.*, vol. 1, no. 1, pp. 2–11, Mar. 2007.

[15] J. G. Pollock, and A. K. Iyer, "Below-cutoff propagation in metamaterial-lined circular waveguides," *IEEE transactions on microwave theory and techniques.*, vol. 61, no 9, p. 3169-3178, 2013.

[16] J. G. Pollock, and A. K. Iyer, "Experimental verification of below-cutoff propagation in miniaturized circular waveguides using anisotropic ENNZ metamaterial liners,", *IEEE Transactions on Microwave Theory and Techniques.*, vol. 64, no 4, p. 1297-1305, 2016.

[17] X. Chen, H. F. Ma, X. Y. Zou, W. X. Jiang, and T. J. Cui, "Three-dimensional broadband and high-directivity lens antenna made of metamaterials", *J. Appl. Phys.*, vol. 110, no. 4, art. no. 044904, Aug. 2011.

[18] A. Bellouch, "Caractérisation et optimisation de structures guidées micro-onde à paroi métamatériau par une méthode de raccordement modal semi-analytique", Ph.D. dissertation., Inst. Nat. Polytechnique de Toulouse, Toulouse, France, 2023.

[19] Y. HU, *et al.*, "All-dielectric metasurfaces for polarization manipulation: principles and emerging applications," *Nanophotonics.*, vol. 9, no. 12, pp. 3755-3780, June. 2020.

[20] A. Krasnok, S. Makarov, M. Petrov, R. Savelev, P. Belov, and Y. Kivshar, "Towards all-dielectric metamaterials and nanophotonics," In *Metamaterials X.*, vol. 9502, p. 950203., SPIE, Mar. 2015.

[21] Y. F. Yu, A. Y. Zhu, R. Paniagua-Domínguez, *et al.*, "High-transmission dielectric metasurface with 2π phase control at visible wavelengths," *Laser Photonics Rev.*, vol. 9, pp. 412–418, 2015.

[22] M. I. Shalaev, J. Sun, A. Tsukernik, *et al.*, "High-efficiency all- dielectric metasurfaces for ultracompact beam manipulation in transmission mode," *Nano Lett.*, vol. 15, pp. 6261–6266, 2015.

[23] A. Zhan, S. Colburn, R. Trivedi, *et al.*, "Low-contrast dielectric metasurface optics," *ACS Photonics.*, vol. 3, pp. 209–214, 2016.

[24] C. Pfeiffer, and A.Grbic, "Metamaterial Huygens' surfaces: tailoring wave fronts with reflectionless sheets," *Physical review letters*, vol. 110, no 19, p. 197401, 2013.

[25] R. Czarny, *et al.*, "High permittivity, low loss, and printable thermoplastic composite material for RF and microwave applications.," *IEEE conference on antenna measurements & applications (CAMA).*, 2018.

[26] K. Singh, M. U. Afzal, M. Kovaleva, and K. P. Esselle, "Controlling themost significant grating lobes in two-dimensional beam-steering systems with phase-gradient metasurfaces.," *IEEE Transactions on Antennas and Propagation.*, vol. 68, no. 3, pp. 1389–1401, 2020.

[27] T. Q. Van Hoang, M. Bertrand, E. Vandelle, and B. Loiseaux, "Low-profile highly directive 2D-beam-steering antenna in Ka-band with 3D-printed all-dielectric sub-wavelength deflectors," in *52nd European Microwave Conference (EuMC).*, pp. 852–855, 2022.

[28] H. CAI, S. Srinivasan, D. A. Czaplewski, *et al.*, "Inverse design of metasurfaces with non-local interactions," *NPJ Computational Materials.*, vol. 6, no 1, p. 116, 2020.

[29] K. Shastri, and F. Monticone, "Nonlocal flat optics.," *Nature Photonics.*, vol. 17, no 1, p. 36-47, 2023.

[30] E. Isnard, S. Héron, S. Lanteri, and M. Elsawy, "Advancing wavefront shaping with resonant nonlocal metasurfaces: beyond the limitations of lookup tables.," *Scientific Reports.*, vol. 14, no 1, p. 1555, Jan 2024.

[31] J. Mockus, "Application of Bayesian approach to numerical methods of global and stochastic optimization.," *Journal of Global Optimization.*, vol. 4, p. 347-365, 1994.

[32] D. R. Jones, M. Schonlau, and W. J. Welch, "Efficient global optimization of expensive black-box functions.," *Journal of Global optimization.*, vol. 13, p. 455-492, 1998.

[33] C. Audet, J. Denni, D. Moore, A. Booker, and P. Frank, "A surrogate-model-based method for constrained optimization.," in *8th symposium on multidisciplinary analysis and optimization*, p. 4891, 2000.

[34] M. J. Sasena, "Flexibility and Efficiency Enhancement for Constrained Global Design Optimization with Kriging Approximations.," PhD thesis, University of Michigan, Michigan, 2002.

[35] D. Huang, T. T. Allen, W. I. Notz, and N. Zeng, "Global optimization of stochastic black-box systems via sequential kriging meta-models.," *Journal of global optimization.*, 2006, vol. 34, p. 441-466, March. 2006.

[36] P. Boyle, "Gaussian Processes for Regression and Optimisation.," PhD thesis, Victoria University of Wellington, Wellington, New Zealand, 2007.

[37] M. Elsawy, *et al.*, "Global optimization of metasurface designs using statistical learning methods.," *Scientific reports.*, vol. 9, no. 1, p. 17918, 2019.

[38] M. Elsawy, S. Lanteri, R. Duvigneau, J. A. Fan, and P. Genevet, "Numerical optimization methods for metasurfaces.," *Laser & Photonics Reviews*, vol. 14, no 10, p. 1900445, 2020.

[39] Z. Liu, D. Zhu, D., S. P. Rodrigues, K. T. Lee, and W. Cai, "Generative model for the inverse design of metasurfaces.," *Nano letters.*, vol. 18, no 10, p. 6570-6576, 2018.

[40] I. Malkiel, M. Mrejen, A. Nagler, U. Arieli, L. Wolf, and H. Suchowski, "Plasmonic nanostructure design and characterization via deep learning.," *Light: Science & Applications.*, vol. 7, no 1, p. 60, 2018.

[41] E. Brochu, V. M. Cora, and N. De Freitas, "A tutorial on Bayesian optimization of expensive cost functions, with application to active user modeling and hierarchical reinforcement learning.," *arXiv preprint arXiv:1012.2599*, 2010.

[42] S. Lanteri, and C. Scheid, "Convergence of a Discontinuous Galerkin scheme for the mixed time-domain maxwell's equations in dispersive media.," *IMA Journal of Numerical Analysis*, vol. 33, no. 2, pp. 432–459, 2013.

[43] J. Viquerat, "Simulation of electromagnetic waves propagation in nano-optics with a high-order Discontinuous Galerkin time-domain method," Ph.D. dissertation, Université Nice Sophia Antipolis, 2015.

[44] DIOGENeS - a Discontinuous-Galerkin based software suite for nano-optics [Online]. Available: https://diogenes.gitlabpages.inria.fr/.

[45] Nanoe - development and fabrication of innovative ceramic materials for the industries [Online]. Available: https://nanoe.com/

[46] T. Q. V. Hoang, J. Sourice, E. Vandelle, R. Faye, M. Bertrand, B. Loiseaux, "Additive manufacturing of a 460mm-diameter flat off-axis lens for ka-band communications," *17th European Conference on Antennas and Propagation EuCAP, IEEE*, p. 1-4., 2023.

[47] M. Bertrand, M. Ettorre, G. Valerio, M. Albani, M., Casaletti, "A broadband low-profile circularly polarized radial line slot antenna," *IEEE Transactions on Antennas and Propagation*, 2022, vol. 71, no 1, p. 140-150.

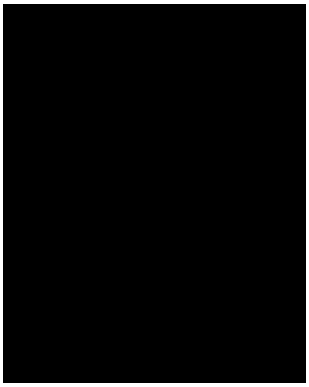

Biography

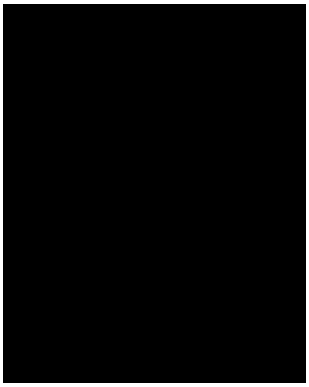

Biography

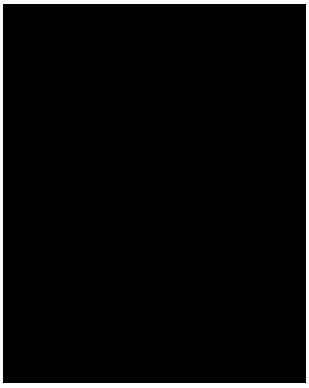

Biography

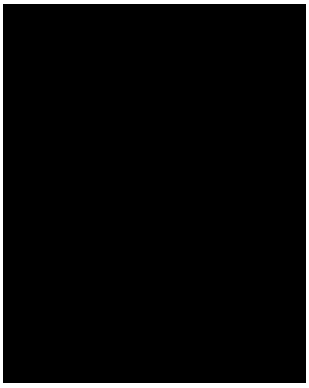

Biography

Table of Contents

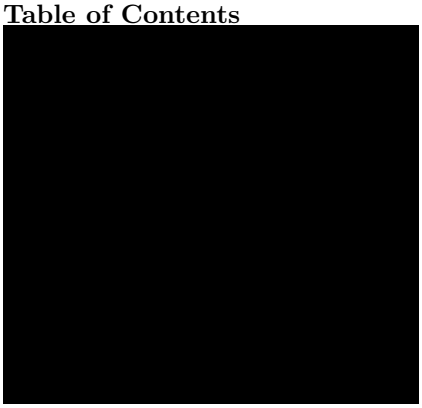

ToC Entry